Received: 3 August 2018 | Revised: 2 December 2019 | Accepted: 2 December 2019

DOI: 10.1002/gj.3727

RESEARCH ARTICLE

WILEY

Magneto-chemical signature of the Lower-to-Middle Siwaliks transition in the Karnali River section (Western Nepal): Implications for Himalayan tectonics and climate

Pitambar Gautam[1] | Pascale Huyghe[2] | Jean-Louis Mugnier[2] | Kamal R. Regmi[3]

[1]Creative Research Institution, Hokkaido University, Sapporo, Hokkaido, Japan

[2]Maison des Géosciences (Bat. IRIGM), Laboratoire de Géodynamique des Chaînes Alpines (UMR 5025), Grenoble, France

[3]Department of Geology, University of Namibia, Pionierspark, Windhoek, Namibia

Correspondence
Pitambar Gautam, Creative Research Institution, Hokkaido University, N21 W10, Sapporo, Hokkaido 001-0021, Japan.
Email: pitambargautam@yahoo.co.jp

Present address
Pascale Huyghe, ISTerre, Universite Grenoble Alpes, CNRS, 38058 Grenoble, France.
Jean-Louis Mugnier, ISTerre, Universite Savoie Mont Blanc, CNRS, 38058 Grenoble, France.

Funding information
Centre National de la Recherche Scientifique, Grant/Award Number: Fellowship; Region Rhone Alpes

Peer Review
The peer review history for this article is available at https://publons.com/publon/10.1002/gj.3727.

Handling Editor: K. Sajeev

Fluviatile sediments comprising a 600-m-thick sequence of the Lower and Middle Siwaliks in the Karnali area in Nepal exhibit a distinct zonation revealed by magnetic and geochemical properties. Four magneto-chemical zones (MCZ1–MCZ4), each about 150 m thick and 400 kyr in duration, provide new insights into Himalayan tectono-climatic events during the Tortonian (Miocene) stage. They exhibit contrasting magnetic susceptibility and isothermal remanence due to differences in magnetic mineral types (magnetite, haematite, and goethite) and concentrations. Odd-numbered zones with higher goethite/(goethite + haematite) ratio, a moisture proxy, indicate wetter conditions in the source area, while the even-numbered zones, virtually without goethite, suggest drier conditions. Chemical indices of alteration/weathering and proxies for hydraulic sorting and mobility derived from the major element compositions also reveal contrasts among these zones. The middle of the MCZ2–MCZ3 zone, with a transitional magneto-chemical signature, is the best candidate for the Lower-to-Middle Siwaliks contact, rather than the field-based boundary placed 18 m up-section at the base of the thick salt-and-pepper sandstone bed. The transition records an increase in river energy and associated accelerated erosion of the Himalayan gneiss zone as the source of coarse-grained material. We suggest a scenario, whereby climate change from drier to wetter (with higher precipitation) conditions affects erosional processes (i.e., weathering, disaggregation and particle transport on the hillslope) prevailing in a large catchment and influencing the depositional modes.

KEYWORDS
chemical index of alteration, climate, geochemistry, goethite, magnetism, Siwalik, Sub-Himalaya

1 | INTRODUCTION

The "chicken or egg" debate (Molnar & England, 1990) outlined the complex interactions between climate and tectonics in the Himalaya and the roles of relief and erosion. The altitude and relief of the Himalaya form an orogenic barrier to atmospheric circulation (Molnar, Boos, & Battisti, 2010; Ruddiman & Kutzbach, 1989), whereas climatically driven erosion influences the location of the deformation between the two moving continental plates (Mugnier et al., 1997). Any tectonic uplift within an orogen is believed to lead to the steepening of topography and disequilibrated longitudinal river gradients (Burbank, Beck, & Mulder, 1996; Leland, Reid, Burbank, Finkel, &

Caffee, 1998). This would force fluvial erosive processes to continually incise and adjust to a longitudinal equilibrium line, leading to massive denudation combined with high sediment flux rates. Numerous isotopic studies of river, delta and Bengal submarine fan sediments indicate that rivers draining the Himalaya contribute a significantly larger share of the dissolved and particulate loads than the rivers draining the Indian shield (Galy & France-Lanord, 2001). The 4-month-long Indian summer monsoon precipitation mainly controls water discharge and 80–95% of the total sediment supply (Barros, Joshi, Putkonen, & Burbank, 2000). This explains the strong variation in seasonal runoff for the large river systems leaving the Himalaya, in which peak flows transport significantly more sediment than that inferred from annual mean discharge (Galy, France-Lanord, & Derry, 1996). Despite much data acquisition and simulation, the nature of these interactions and the relative importance of climatic, tectonic, and associated uplift and erosional phenomena remain controversial, partly due to the lack of detailed field-based physico-chemical records from the fluvial foreland basin, delta plain and submarine fan deposits in support of plausible interpretations (Clift et al., 2008; Galy & France-Lanord, 1999; Huyghe, Galy, Mugnier, & France-Lanord, 2001; Kutzbach, Prell, & Ruddiman, 1993; Larson, Godin, & Price, 2010; Whipple, 2009).

The Siwalik Group, comprised of fluvial clastic sediments of Mio–Pliocene age derived mainly from the erosion of the Himalayan mountain range, is an important archive of physico-chemical records related to complex interactions among climate, tectonics, and erosional processes. This group is exposed along the Sub-Himalaya, which represents the former foreland basin at the southern margin of the 2,500-km-long Himalayan arc (Figure 1). The large-scale geometry of the foreland reflects the progressive flexure of the Indian crust induced by the Himalayan thrust motion (Burbank et al., 1996; Mugnier & Huyghe, 2006), whereas its sediments record both the southward migration of the Himalayan front (Delcaillau, Hérail, & Mascle, 1987) and paleoenvironmental/climatic events. The threefold Upper, Middle, and Lower Siwaliks (LS, MS, and US) classification, used for informally subdividing the foreland basin sedimentary units since the work of Medlicott (1864), remains a key for analysing the sediment cores and describing the geological units (e.g., the data repositories in Hirschmiller et al., 2014 and Mugnier & Huyghe, 2006).

Significant regional lithological variation and structural/tectonic complexity and the lack of index fossils within the Siwalik Group in Nepal pose challenges for mapping and geochronological studies. As a result, besides the threefold nomenclature (LS, MS, and US) used by Gansser (1964), Glennie and Ziegler (1964), Itihara, Shibasaki, and Miyamoto (1972), DMG (1978), and Herail and Mascle (1980), regional or local lithostratigraphic schemes comprising four- or fivefold divisions (Corvinus, 1988; Nakayama & Ulak, 1999; Tokuoka, Takayasu, Yoshida, & Hisatomi, 1986; Upreti, 1999) are used. The first

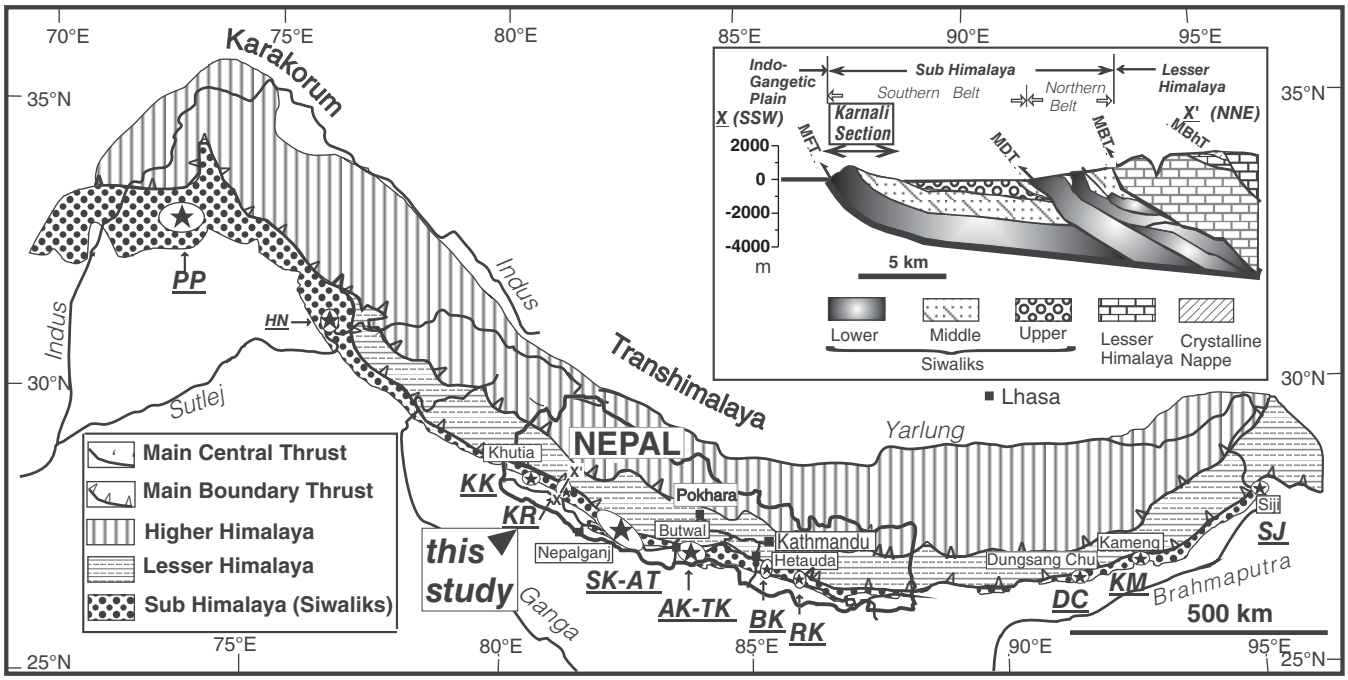

FIGURE 1 Schematic map of the Himalayas showing the main structural zones and the location of the Karnali River section including the Lower Siwaliks (LS) to Middle Siwaliks (MS) transition studied. Stars indicate selected areas of past magnetostratigraphic and related studies by different research teams, indicated by abbreviated name (section identification): KK (Khutia Khola), KR (Karnali River), SK–AT (Surai Khola–Amilia Tui), AK–TK (Arung Khola–Tinau Khola), BK (Bakiya Khola), and RK (Rato Khola) in Nepal; DC(Dungsam Chu) in Bhutan; KM (Kameng) and SJ (Siji), HN (Haritalyangar) in India; and PP (Potwar Plateau) in Pakistan. The inset shows the geotectonic zones (Indo-Gangetic Plain, Sub-Himalaya, and Lesser Himalaya) and belts separated by major discontinuities (MFT: Main Frontal Thrust, MDT: Main Dun Thrust, MBT: Main Boundary Thrust, and MBhT: Mahabharat Thrust) along line X–X' parallel to the KR traverse. Modified from Gansser (1964) and Gautam and Fujiwara (2000)

magnetostratigraphic ages (Munthe et al., 1983; Tokuoka et al., 1986) and detailed maps (Tokuoka et al., 1986, 1990) revealed that lithological units with identical threefold nomenclatures could be of largely differing ages. This led to the use of local lithostratigraphic schemes, if available, to tie up a newly obtained magnetostratigraphic chronology.

This paper deals with a local but precise study of the transition zone containing a regional and syn-orogenic lithologic boundary between LS and MS within the Karnali River section in Nepal (Figure 1). Described long ago by Medlicott (1864), the LS–MS boundary accompanied by a transitional zone is an important lithological/chronological marker of Himalaya-wide changes throughout the Sub-Himalaya from the Potwar Plateau (e.g., Johnson, Opdyke, Johnson, Lindsay, & Tahirkheli, 1982) to Arunachal (e.g., Chirouze et al., 2012; Coutand et al., 2016; Lang, Huntington, Burmester, & Housen, 2016). The LS–MS transitional zone is important due to its affinity to the inferred timing of establishment of the monsoonal precipitation pattern currently affecting the southern Himalayan front. This establishment occurred between ca. 12 Ma (15–10 Ma, when the Tibetan Plateau attained a threshold elevation sufficient to block the penetration of moisture from the Indian Ocean and from the south Pacific into western China and caused a reorganization of atmospheric circulation pattern) and 9–8 Ma (when a shift to a monsoonal circulation system similar to that of today was already in place) (Dettman et al., 2001; Garzione, Dettman, Quade, DeCelles, & Butler, 2000; Molnar, England, & Martiod, 1993; Prell & Kutzbach, 1992; Ruddiman & Kutzbach, 1989; Spicer, 2017; Zhisheng, Kutzbach, Prell, & Porter, 2001). This study focuses on a 600-m-thick Karnali River subsection in which the LS–MS boundary displays rock-magnetically significant variation (Gautam, Hosoi, Regmi, Khadka, & Fujiwara, 2000). To decipher the records of climate, uplift, and other related phenomena at the transition close to the LS–MS boundary, it describes new magnetic and chemical evidence that complements the geological, sedimentological and petrographic observations (Huyghe, Mugnier, Gajurel, & Delcaillau, 2005; Sigdel & Sakai, 2013; Sigdel, Sakai, Ulak, Gajurel, & Upreti, 2011).

2 | THE LS–MS BOUNDARY IN THE KARNALI RIVER SECTION

The Karnali River section in Western Nepal is unique in its continuity of exposures, lithological diversity, the long age span of the sediment sequence, and the availability of a diverse set of geoscience data (Dhital, 2015; Galy & France-Lanord, 2001; Gautam & Fujiwara, 2000; Huyghe et al., 2001; Huyghe et al., 2005; Mugnier, Delcaillau, Huyghe, & Leturmy, 1998). It comprises 6,285 m of sediments (LS or Chisapani Formation, 2,045 m; MS or Baka Formation, 2,740 m; US or Kuine and Panikhola formations, 1,500 m) within the Southern Belt of the Sub-Himalaya (Gautam & Fujiwara, 2000; Sigdel et al., 2011) (Figure 2). Magnetostratigraphic ages from this section helped constrain the chronology of newly mapped lithostratigraphic units and geologic formations, fission-track data, and tectonic and paleoenvironmental/climatic events in the foreland basin as well as in the Himalayan hinterland (Baral, Lin, & Chamlagain, 2017; Bernet et al., 2006; Gautam, 2008; Gautam & Fujiwara, 2000; Gautam, Ulak, Paudayal, Gyawali, & Bhandari, 2012; Huyghe et al., 2005; Najman, 2006; Neupane et al., 2017; Sigdel et al., 2011; Sigdel & Sakai, 2013; Szulc et al., 2006; van der Beek et al., 2006, 2016).

Two contrasting hypotheses exist for the placement and dating the LS–MS contact in Nepal. One of them puts the LS–MS contact at the base of the first prominent thick bed of medium- to coarse-grained, salt-and-pepper type sandstone (hereafter, spss), leading to an age of <10 Ma, as proposed for the Karnali River section. This hypothesis agrees closely with several other studies on sections in areas of Surai Khola (Appel, Rösler, & Corvinus, 1991; Dhital, Gajurel, Pathak, Paudel, & Kizaki, 1995), Tinau Khola South (Gautam & Appel, 1994), Amilia-Tui (Rösler, Metzler, & Appel, 1997), and Arung Khola-Binai Khola (Gautam et al., 2012; Tokuoka et al., 1986, 1990). Another hypothesis places the LS–MS contact at the first appearance of the coarse-grained or so-called "multi-storied" sandstone, as applied to the Khutia Khola, Tinau Khola South and Surai Khola sections (Ojha et al., 2000; Ojha, Butler, DeCelles, & Quade, 2009), leading to an age of the contact at around 11 Ma. Due to differences in these hypotheses, there may be significant differences in the position and timing of the so-called "LS–MS boundary," even for the same section; for example, in the case of Surai Khola, there is an approximately 300 m (equivalent to about 1 myr) difference in the position (age) of the top of LS in lithostratigraphic columns published by various authors. Even larger differences in position and age for variously defined but similarly named informal unit boundaries (LS–MS and MS–US) are possible among different sections mapped and dated by different author(s). Caution is needed, therefore, during stratigraphic correlations not to translate such false age discrepancies for the Siwalik units and their boundaries to apparent temporal differences in associated Himalaya-wide tectonic and paleoenvironmental/climatic events.

In the Karnali area, the LS sequence represents a rhythmic alternation of mainly fine-grained quartzose, partly calcareous sandstones, and commonly variegated mudstones. The MS sequence represents an alternation of sandstone, generally medium- to coarse-grained, grey, and mica-rich (with a salt-and-pepper appearance resulting from a mixture of white muscovite and black biotite flakes) and mudstone (mostly non-variegated), where the sandstone occurs in higher proportion. The LS–MS boundary, defined after Rösler et al. (1997) and Mugnier et al. (1998), falls at the 2,015 m level, corresponding to the base of the first prominently thick (>5 m), medium- to coarse- grained spss sequence (Gautam & Fujiwara, 2000). Subsection C (Figure 2) includes the rock-magnetic "middle segment," with a long-wavelength low-field volume susceptibility signal, fluctuating between 5×10^{-5} and 2×10^{-4} SI and linked to possible long-term climatic changes in the Himalayan source region and/or the depositional basin (Gautam et al., 2000). It includes the sediments of the uppermost LS and the lowermost MS, which correspond to the Upper Chisapani Formation and the lower half of the Lower Baka Formation of Sigdel et al. (2011).

Huyghe et al. (2005) described the sedimentary facies association in the Karnali section. The upper LS consists of alternating medium- to coarse-grained grey sandstone beds and thinner sequences of fine-grained muddy sandstone and mudstone beds, where the basal

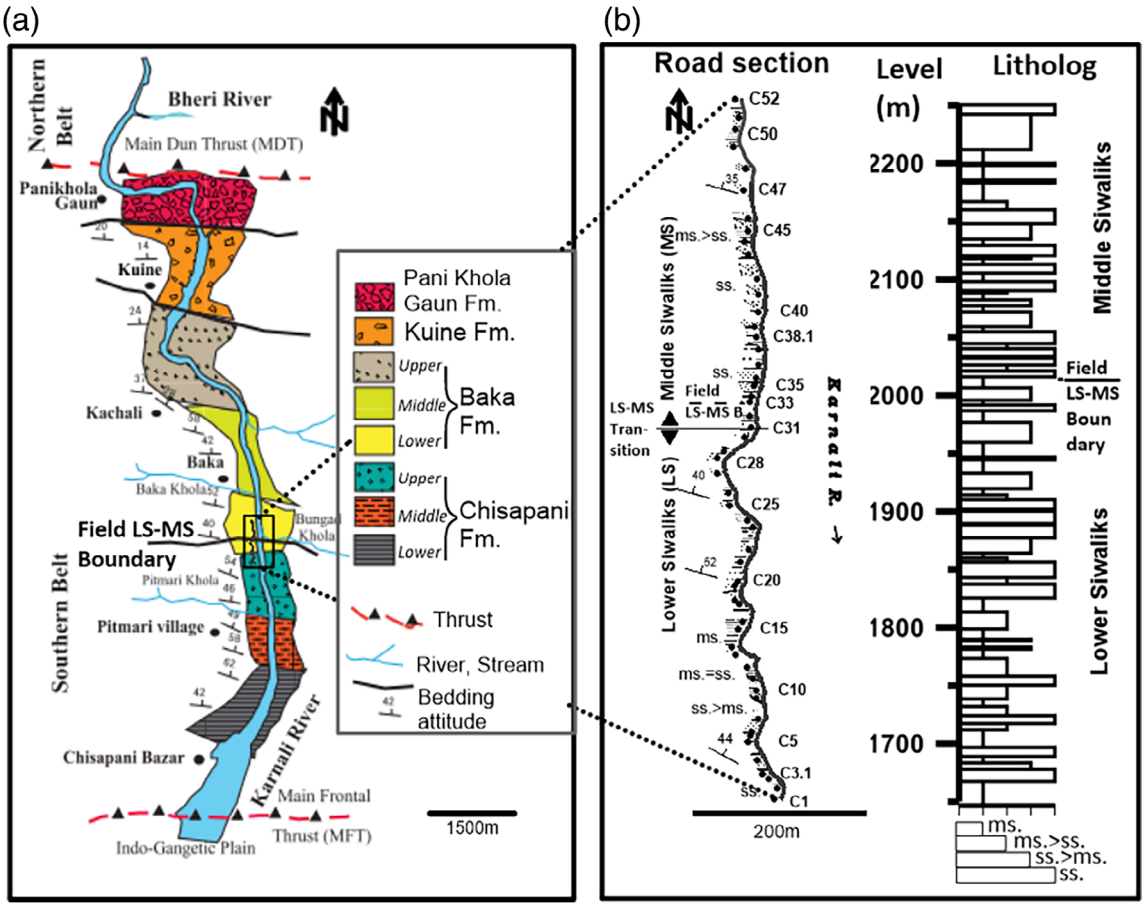

FIGURE 2 (a) Local geologic divisions of the Siwalik Group along the Karnali River (modified from Sigdel & Sakai, 2013). The Lower Siwaliks (LS) and Middle Siwaliks (MS) in Gautam and Fujiwara (2000) correspond to the Chisapani and Baka formations, respectively. (b) Simplified geologic route map, with sampling sites/levels, along the road on the right bank of the Karnali River, with the lithostratigraphic column corresponding to the 1,650–2,250 m section (sector C of Gautam & Fujiwara, 2000). The LS–MS transition lies 18 m downward from the base of the very thick salt-and-pepper sandstone sequence at C31—the centre of the transitional zone that records the significant changes in magneto-mineralogical and geochemical parameters

surface of coarser grained sandstone beds is erosional. The facies association in the lower MS was described to have contrasting features: (a) abundance of light-grey, thick and coarse- to very coarse-grained horizontal and trough cross-stratified sandstone beds containing a lot of muscovite; (b) occurrences of pebbly sandstones and interbedding of grey-brown to grey-green mudstones; and (c) the presence of coarse sandstone beds, each ~10 m thick, with non-erosional planar basal surfaces and bottoms containing multi-decimetric lenses of laminated clays and paleosols. The LS sediments were deposited by a meandering system with increasing discharge, while MS sediments were formed by a sandy braided system. Based on isotope geochemistry, the upper part of the LS represents an equilibrate mixture of sediments originating from the Lesser and High Himalayas, but the MS reflects mainly the High Himalayan provenance.

Gautam and Fujiwara (2000) assigned the lower 3,560 m of the Karnali River section a depositional age range of 15.8–6.2 Ma, using the geomagnetic polarity time scale of Cande and Kent (1995) (CK95). The present subsection (Figure 2b) and the LS–MS boundary according to CK95 correspond to about 10.60–9.15 Ma, and 9.6 Ma, respectively. Renewed magnetostratigraphic correlation of the subsection to the astronomically tuned Neogene time scale of Lourens, Hilgen, Laskar, Shackleton, and Wilson (2004) (ATNTS2004) would shift the age span to 10.71–9.32 Ma, with the lower and upper boundaries becoming 0.11 myr and 0.17 myr older, respectively. To avoid confusion, the age interpretations hereafter follow CK95, with limited references to ATNTS2004. Lithological changes, the geological nomenclature, and the sandstone petrography along the subsection are given in Appendix S1.

3 | LABORATORY PROCEDURE AND METHODS OF ANALYSIS

Thirty-four cores, 2.54 cm in diameter and 2.2 cm long, of relatively fresh siltstone and fine-grained sandstone, obtained as sister samples cut from the long independently oriented cores drilled for magnetostratigraphic study along the road at the right bank of the Karnali River (Figure 2), were used for laboratory measurements. Although the clastic sediments exhibited a wide grain-size range, our analysis

was restricted to siltstones and fine-grained sandstones to ensure that the geochemical indices were reasonably free from changes due to systematic grain-size variation and lithological composition dependent on the stratigraphic position. Measurements and analyses were grouped into two types (rock-magnetic and geochemical), described separately below.

3.1 | Rock-magnetic measurements

Laboratory rock-magnetic measurements, made at the paleomagnetic laboratory of CEREGE, France, were as follows.

3.1.1 | Magnetic susceptibility

At least one specimen from each sampling level was measured for the low-field volume magnetic susceptibility (κ_{lf}) using the AGICO KLY-3 Kappabridge. For subsequent interpretation, κ_{lf} was recalculated to the mass-specific magnetic susceptibility (χ_{lf}) after dividing by the mass of the specimen.

3.1.2 | Isothermal remanent magnetization (IRM) acquisition and back-field demagnetization

Every sixth specimen was subjected to IRM acquisition at discrete fields using a magnetic measurements pulse magnetizer. The discrete fields were selected considering the contributions from soft, intermediate and hard-coercivity magnetic minerals (Gautam et al., 2000). The saturation IRM (SIRM) acquired after each magnetization step was measured by using the SQUID device. The SIRM achieved at 3 T was subjected to alternating field (AF) demagnetization (with 5 mT steps between 50 and 100 mT, rarer steps outside this range) to accurately determine the median destructive field (MDF), defined as the peak AF required to reduce the IRM moment to half its initial value. Chips and powder specimens from core specimens at several sites were subjected to high-field IRM acquisition using direct-current (DC) pulse fields of up to 9 T.

To estimate the relative contributions of magnetic minerals with different coercivities, however, all other specimens were subjected to IRM acquisition at three steps, 0.3 T, 1.5 T and 3 T. Acquisition and back-field destructions of remanence were conducted on discrete chip samples by applying a maximum field of 1 T using the vibrating sample magnetometer (Micromag). The hysteresis curves were analysed for saturation magnetization, saturation remanent magnetization, and coercivity of remanence, indicative of the magnetic mineralogy and grain-size characteristics.

3.2 | Geochemical analyses

From each sampling site/level, at least one sample used for non-destructive IRM measurements was subjected to a chemical analysis for major oxides. Each sample was first powdered in an agate mortar. Major element concentrations were measured by ICP-AES at "Service d'Analyse des Roches et des Minéraux" (SARM – CRPG, Nancy-France) from bulk aliquots of 100 mg, following analytical procedures developed by Govindaraju and Mevelle (1987). The relative uncertainty for major elemental concentrations was better than 2%.

Major oxide compositions of ancient and modern clastic sediments have been commonly used to infer the source rocks, provenance and tectonic setting (McLennan, Hemming, McDaniel, & Hanson, 1993; Nesbitt & Young, 1982; Rahman & Suzuki, 2007). The aim of the geochemical analyses was to discriminate different segments of the lithostratigraphic column by the geochemical behaviour of sediments reflected in the compositional variation in elements, oxides and their ratios. The sediment behaviour, governed by source area rock composition related to tectonic setting, transport and concomitant grain-size changes, in situ diagenesis, and weathering, was examined by using limited indices and bi-plots derived from various combinations of oxides (wt.%) of major elements and their molar ratios, as briefly described below.

3.2.1 | Loss on ignition

Loss on ignition (LOI) may be used as a proxy of sediment hydration. In continental detrital environments (e.g., the Ganga Basin sediments), Lupker, France-Lanord, Galy, Lave, and Kudrass (2013) found it to be a sensitive tracer of silicate weathering.

3.2.2 | Chemical index of alteration

This index is calculated using the molar proportions of oxides as follows:

$$CIA = 100{*}Al_2O_3/(Al_2O_3 + CaO{*} + Na_2O + K_2O),$$

where CaO* is equal to either to the concentration of CaO (for CaO ≤ Na_2O), or of Na_2O if the opposite is true, following McLennan et al. (1993). In this calculation, apatite-bound Ca is assumed to be negligible.

Chemical index of alteration (CIA) values range from 1 to 100, with the value directly reflecting the degree of chemical weathering that caused the degradation of silicates (particularly feldspars) in rocks and sediments and the formation of secondary clay minerals, resulting in changes in the proportions of major elements (water-immobile Al relative to Na, K, and Ca) in the material affected by weathering.

3.2.3 | Chemical index of weathering

Cullers (2000) and Buggle, Glaser, Hambach, Gerasimenko, and Markovic (2011) proposed the chemical index of weathering (CIW) as a proxy of alteration independent on the concentrations of Ca and K

cations and thus insensitive to bias effects caused by CaO originating from minerals other than silicates. It is calculated as follows:

$$CIW = 100 \times Al_2O_3/(Al_2O_3 + Na_2O)$$

Like the CIA, CIW values range from 1 to100, where a higher value indicates more intense weathering of the rocks in the source area.

3.2.4 | Miscellaneous bi-plots reflecting chemical composition, grain size, and element mobility

To discriminate the different segments of the column, CIA, CIW and several other oxide ratios were calculated and plotted against each other in several diagrams to determine the most "effective" complex of indicators when considered in combination with the magnetic parameters. Several bi-plots involving TiO_2, Na_2O, K_2O, Al_2O_3, SiO_2, Fe_2O_3, ΣBases, and Si-normalized ratios of Fe and Al were considered as follows.

Al_2O_3 (wt.%) vs. SiO_2 (wt.%)

Fe_2O_3 (wt.%) vs. TiO_2 (wt.%)

ΣBases (wt.%) vs. TiO_2 (wt.%)

ΣFe/Si [mol] vs. Al/Si [mol]

K/Si [mol] vs. Al/Si [mol]

In a study of loess-palaeosol sequences, Schatz, Scholten, and Kühn (2014) found the first three plots useful in detecting pedogenesis-related relative enrichment of Al and Fe. The third plot helps to determine the loss of bases. Lupker et al. (2011) suggested the last two relationships to ascertain the role of hydraulic sorting and the intensity of chemical weathering leading to the loss of mobile elements. According to Galy and France-Lanord (2001), dissolved Si and Al represent only ca. 1% and less than 0.1%, respectively, of the particulate flux in the Himalayan system, and these elements can thus be treated as immobile, to a first approximation. Chemical weathering therefore seems to result in the loss of the most mobile elements such as Na, K, Mg, and Ca at constant Al/Si for steady-state weathering.

4 | DATA ACQUISITION, PROCESSING, AND PRESENTATION OF RESULTS

4.1 | Geochemistry of sediments

4.1.1 | Chemistry of major oxides

Data on the major oxide composition (wt.%) for the samples analysed are given in Table A1 (supplementary material). For 34 samples, LOI (wt.%) ranged from 5.9 to 23.7, with an average of 14.9 ± 4.1. LOI reflects the variable amounts of carbonate, hydrous phases such as clay minerals, and organic matter in sediments. LOI tends to increase due to mineral hydrolysis and neoformations associated with weathering reactions in the flood environment (Lupker et al., 2013). However, six samples of Sigdel and Sakai (2013) (their sample C21 corresponding to C2 in this study, and another five samples [C22, C24, D1, Bk-23, D2] situated between C22 and C52 of this study) taken from the same or an equivalent newly exposed section yielded CaO (wt.%) values from 7.1 and 23.1 (Table A1 in Appendix S1), and modal CO_3 (volume %) values from 11.0 to 23.8 (Table 2 in Sigdel & Sakai, 2013), implying a strong relation to carbonates. A plot of CaO (wt.%) versus LOI reveals a high positive correlation (R^2 = 0.95), indicating that LOI is mainly associated with carbonates (Figure 3).

The major oxide concentrations (wt.%) recalculated on an anhydrous basis, the molar ratios of oxides, and various indices related to chemical alteration and weathering are given in Table A2 (Appendix S1). These data show the mutual relationships among oxides, elements, and derived indices.

4.1.2 | Weathering and alteration indices

In the A-CN-K diagram (Figure 4), the CIA computed with CaO* discriminates the LS and MS subsections above and below C31, which has an intermediate position. The samples plot parallel to the A–CN axis (i.e., the line connecting Al_2O_3 with CaO + Na_2O), following a nearly ideal weathering trend.

In Figure 5, two diagrams depict the relationship between the CIA and CIW. There is a high positive correlation (R^2 = 0.95) between CIA (%) calculated with CaO* and CIW (%) that is independent of Ca and K. These data (Figure 5a,b) show that the calculated CIA is a valid proxy for chemical weathering of the source rocks. Uncorrected CaO only weakly correlates with the CaO-based weathering index (CIA)

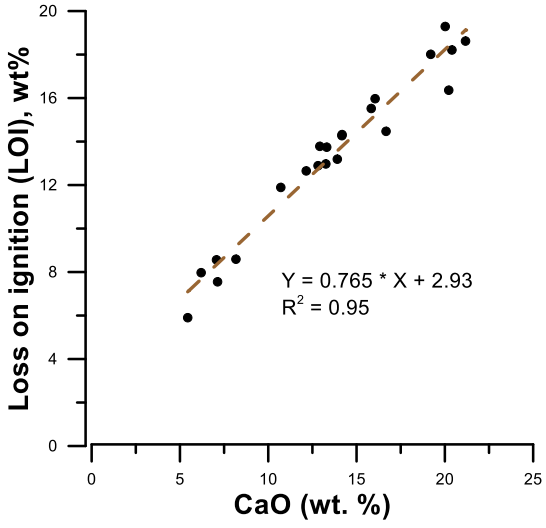

FIGURE 3 A bi-plot of loss on ignition (LOI, wt.%) against calcium oxide (CaO, wt.%) showing a high positive correlation

(R^2 = 0.38), implying that CIA variation may not be strongly influenced by uncorrected CaO.

Figure 6 shows additional bi-plots of major oxide chemistry (anhydrous basis) between the LS and MS subsections. Although the samples from these subsections show a tendency to plot in areas without much overlap, the linear regression lines that apply to all data points show only moderate correlations. The Fe_2O_3(T) versus TiO_2 diagram (Figure 6b) shows better linear correlation as well as discrimination power than the sum of bases (wt.%) versus TiO_2 (wt.%) diagram (Figure 6a).

Figure 7 shows the plots depicting the proxies of hydraulic sorting and the intensity of chemical weathering reflecting the loss of mobile elements. Al/Si ratio, plotted along the horizontal, is used as a proxy of mineral sorting effects. It strongly correlates with grain size. Coarse-grained sediments are enriched in quartz and have thus a low Al/Si ratio while finer grained surface sediments tend to be enriched in phyllosilicates and clay minerals that have higher Al/Si ratios. This scenario resembles the situation in a water column in which the sediments with a range of Al/Si ratios and hydrodynamic mineral sorting would result in a binary mixing trend between two end-members characterized respectively by a low Al/Si (coarse-grained) and a high Al/Si (fine-grained) ratio (Lupker et al., 2011).

In the ΣFe/Si versus Al/Si plot (Figure 7a), MS samples lie close to line segment with relatively coarse grain size and poor sorting. The opposite is true for the LS samples, which are finer and better sorted. The upper end of the fitted line is directed toward clays (phyllosilicates), but lower end toward quartz. In the K/Si versus Al/Si plot, the LS and MS subsections show significant variation in the relative concentration of the mobile element K. Unlike in several earlier plots (Figures 4–6), there is a significant overlap in samples from the two subsections. This may be due to periodic or quasi-periodic variation in these proxy ratios at relatively low time and thickness scales.

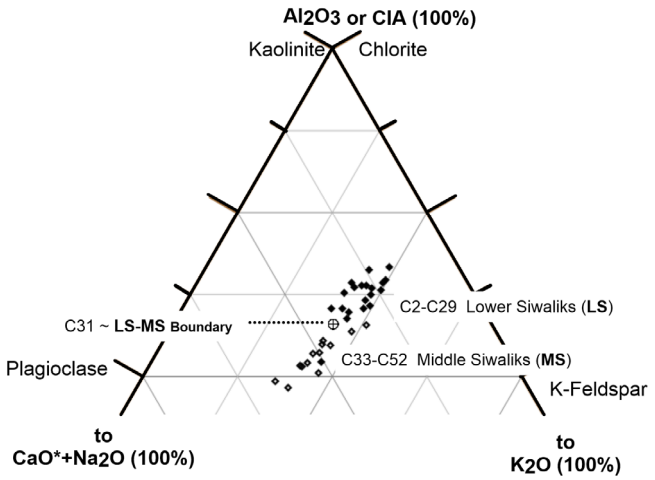

FIGURE 4 Ternary diagram showing the chemical index of alteration (CIA) computed with CaO* (amount of CaO incorporated in the silicate fraction) to discriminate the Lower and Middle Siwaliks subsections above and below sampling level C31

4.2 | Rock-magnetic properties

4.2.1 | Low-field magnetic susceptibility

The magnitude of volume magnetic susceptibility (κ_{lf}) depends on the mineralogy comprising ferro/ferrimagnetic (e.g., magnetite or maghemite, 2–3 SI; haematite, $\leq 6 \times 10^{-3}$ SI; goethite, about 3.5×10^{-3} SI), paramagnetic (mica and amphiboles, 10^{-4} SI; pyroxenes, $0.5–5 \times 10^{-3}$ SI; tourmaline, 1.69×10^{-3} SI, etc.), and diamagnetic (e.g., quartz, calcite, feldspars, about -14×10^{-6} SI) minerals, varying between 10^{-5} and 10^{-2} SI owing to complex contributions by all of them (Gautam & Rösler, 1999). Sediment with abundant

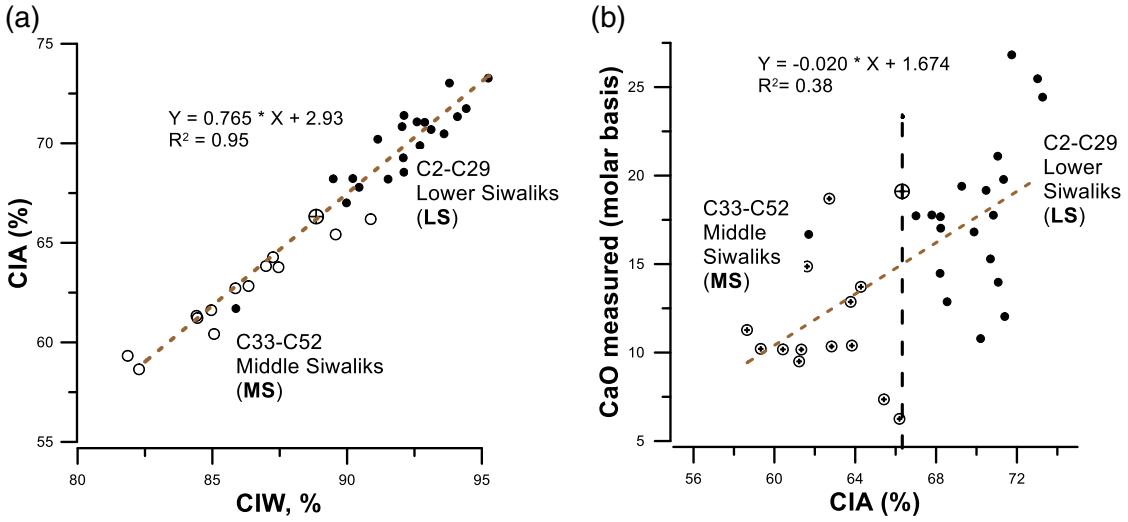

FIGURE 5 Bi-plots showing strong relationships among the chemical alteration and weathering indices that clearly differentiate the Lower and Middle Siwaliks subsections. (a) CIA (%) calculated with CaO* versus CIW (%) free from Ca and K. (b) CaO (wt.%) versus CIA (%) plot showing weak overall correlation, but two distinct LS (Lower Siwaliks) & MS (Middle Siwaliks) subsets

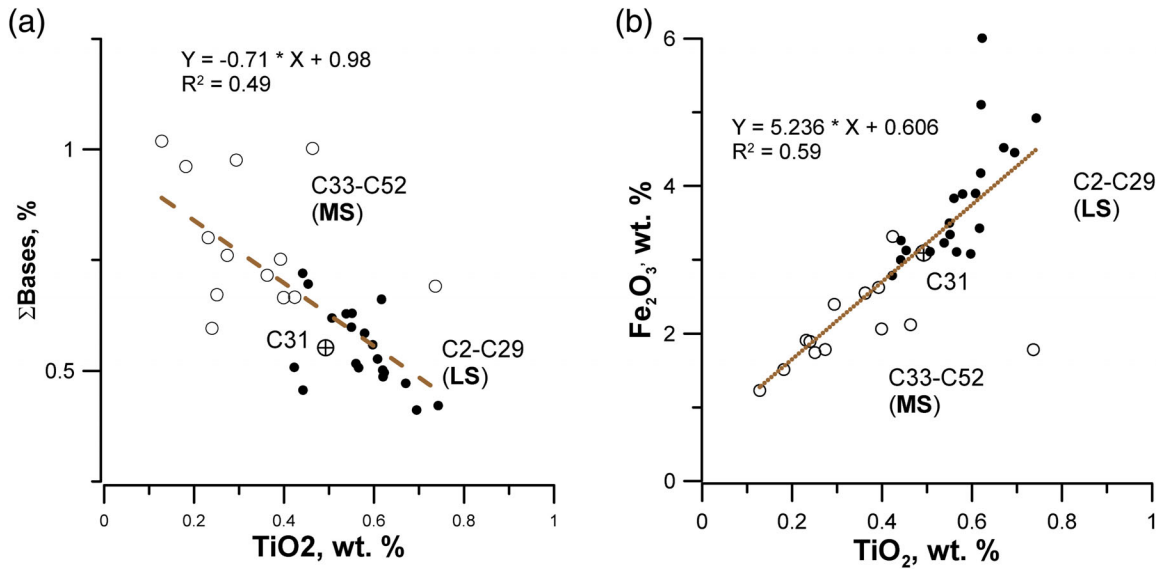

FIGURE 6 Bi-plots showing mutual variation in major oxide chemistry (anhydrous basis) between the LS and MS subsections. (a) Sum of bases (wt.%) versus TiO_2 (wt.%). (b) Fe_2O_3(T) versus TiO_2

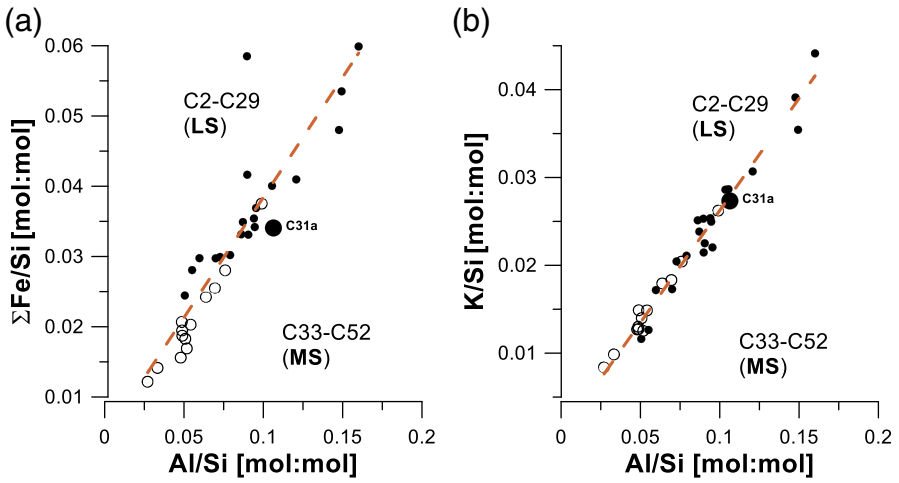

FIGURE 7 Bi-plots showing the variation in ΣFe/Si versus Al/Si molar ratios as a proxy for (a) hydraulic sorting, and (b) K/Si versus Al/Si molar ratios as a proxy of the intensity of chemical weathering leading to loss of mobile elements

paramagnetic particles has low κ_{lf}, whereas medium-grained spss yields higher values (≥300 × 10^{-6} SI). In general, κ_{lf} averaged for sedimentary cycles increases stratigraphically upwards in each Siwalik section, in line with the coarsening- and thickening-upward trend of the sandstones and a proportional increase in the contribution of ferrimagnetic minerals (maghemite and magnetite) in the same direction. Within each sedimentary cycle that begins with coarser sandstone and ends up in finer mudstone, κ_{lf} decreases upward except for cases of variegated sediments locally enriched in magnetic minerals. Haematite, mainly of detrital origin, is present in the whole sequence and is responsible for the stable depositional remanence. Pigmentary haematite (common in variegated sediments), maghemite and magnetite (occurring in sandstones from the upper parts), and goethite formed partly due to weathering-related processes in the present day environment carry secondary remanences (Gautam & Fujiwara, 2000; Schwertmann, 1988; Taylor & Schwertmann, 1974). The subsection studied includes an anomalous susceptibility variation that coincides with the LS–MS transition (Gautam et al., 2000). A new set of samples was used to reconstruct this variation in susceptibility expressed in mass-specific units.

4.2.2 | Isothermal and back-field remanences

IRM acquisition experiments employing DC pulses of up to 2.5 T on the siltstones and sandstones indicated the presence of a substantial amount of a hard-coercivity goethite (partial loss of remanence upon heating up to 150°C), in addition to moderate-coercivity haematite and magnetite/maghemite of soft but varying coercivity range. Because of the typical range of the unblocking/demagnetization temperature and/or the IRM acquisition field range of each of these minerals, several different ratios of rock-magnetic and remanence

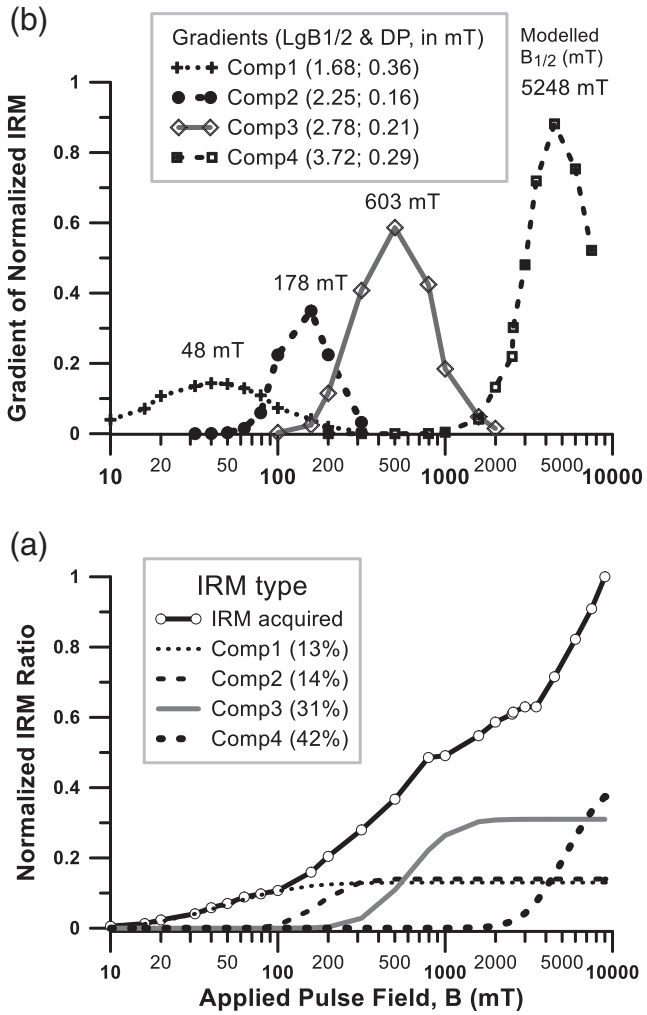

FIGURE 8 Example of magneto-mineralogy inferred from the isothermal remanence acquisition (IRM) curve of a typical chip sample (C24). (a) Total IRM curve and its log-normal decomposition into four components saturating at increasingly high fields. (b) Gradient curves corresponding to components of varying coercivities (soft, intermediate, hard and very hard) with well-defined median destructive field (MDF: 48 mT to 5.3 T) and dispersion (half-widths) parameters. These components with increasing coercivities were inferred to correspond to magnetite-like, maghemite-like, haematite, and goethite phases

parameters could be used to estimate the relative remanence contribution and trace the variation in each mineral along the stratigraphic column.

A complete IRM component analysis, for a representative sample, following Kruiver, Dekkers, and Heslop (2001) revealed four components with MDFs 48 mT, 178 mT, 603 mT, and 5.3 T (Figure 8a,b). These MDFs were attributed to magnetite-like, maghemite-like, haematite and goethite phases, respectively. In the high-field IRM acquisition curves for three chip samples subjected to discrete fields up to 9 T, the steep slope portion corresponding to IRM acquired at fields above 1.5 T represents the contribution of a hard-coercivity mineral corresponding to goethite (Figure 9a). Whereas samples C14 and C42 attain saturation by 6 T, C24 shows no tendency to saturate even at 9 T, and this is consistent with the MDF of about 5.3 T (Component 4 in Figure 8). Rochette et al. (2005) noted that goethite may exhibit extreme remanence coercivities, and the remanence acquired at 3 T may be only 2–10% of the 57 T remanence of pure goethite. Goethite in our samples, however, was found to attain reasonable saturation by fields of 9 T. Three curves obtained by the back-field demagnetization of "saturation magnetization" acquired at 1 T, as a part of hysteresis measurements, yielded the coercivity of remanence range (0.32–0.38 T) suggestive of a highly variable contribution of hard (high-coercivity) minerals (Figure 9b).

4.2.3 | Vertical profiles of IRM components and paleoenvironmental proxies

IRM components reflecting relative contributions of the minerals with varying coercivities were calculated as follows (Gautam et al., 2000; Rösler & Appel, 1998):

Soft: IRM(0.3 T)/IRM(3 T).
Intermediate: [IRM(1.5 T) − IRM(0.3 T)]/IRM(3 T).
Hard: [IRM(3 T) − IRM(1.5 T)]/IRM(3 T).

IRM magnitudes were used to calculate contributions of goethite, haematite, and a paleoenvironmental proxy for relative goethite content, in agreement with studies on terrestrial sediments of the Siwaliks in India (Sangode & Bloemendal, 2004) and Bengal fan deposits (Abrajevitch, van der Voo, & Rea, 2009), as follows:

Goethite estimate: Gth* = [IRM(3 T) − IRM(1.5 T)]/SIRM(goethite).
Haematite estimate: Hmt = [IRM(1.5 T) − IRM(0.3 T)]/SIRM (haematite).
Relative goethite content: (Gth*/(Gth* + Hmt).

In these expressions, SIRMs for goethite and haematite are taken as 2.0 kA/m and 2.5 kA/m, respectively, ignoring the effects of possible grain size and admixtures (Dunlop & Özdemir, 1997, p. 51). The Gth* contribution is often an underestimate due to the lack of saturation of the goethite-based IRM by 3 T. In such a case, the Gth*/(Gth* + Hmt) ratio may be underestimated, but the general trend of variation along the section will be preserved (Abrajevitch et al., 2009). Similarly, the ratio of IRM(0.3 T)/SIRM(magnetite), with the SIRM of 480 kA/m for pure magnetite, may be a minimum estimate for the "effective magnetite" concentration. "Effective magnetite" includes maghemite (SIRM: 380 kA/m) and titanomagnetite or even greigite (each with a maximum SIRM of 125 kA/m) (Dunlop & Özdemir, 1997, p. 51), all of which exhibit soft coercivities.

Selected magnetic parameters (mass-specific magnetic susceptibility (χ_{lf}); IRM(3 T) to χ_{lf} ratio; IRM components; estimates of haematite, goethite, and the goethite to "combined hematite and goethite" ratio for samples along the section are compiled in Table A3 (Appendix S1) and shown in Figure 10.

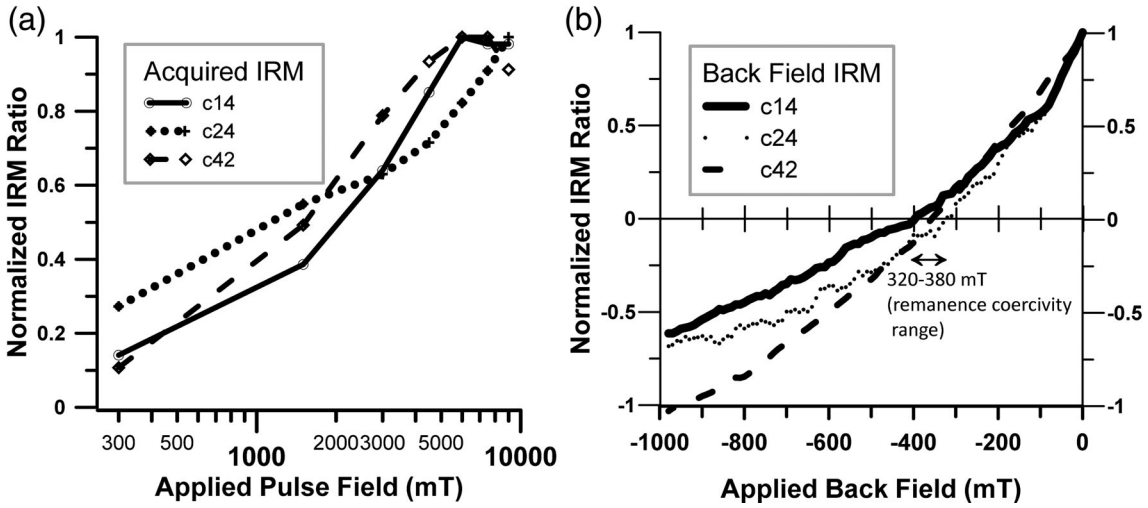

FIGURE 9 High-field (up to 9 T) IRM acquisition (a) and back-field demagnetization of "saturation remanence" acquired at 1 Tesla (b) for three samples representative of the whole subsection. In (a), the steep slope portion generally above 2–3 T represents the contribution of a very hard-coercivity mineral (goethite). The coercivity of remanence range (0.32–0.38 T) derived from the back-field curves (b) suggests a highly variable contribution of hard (high-coercivity) minerals

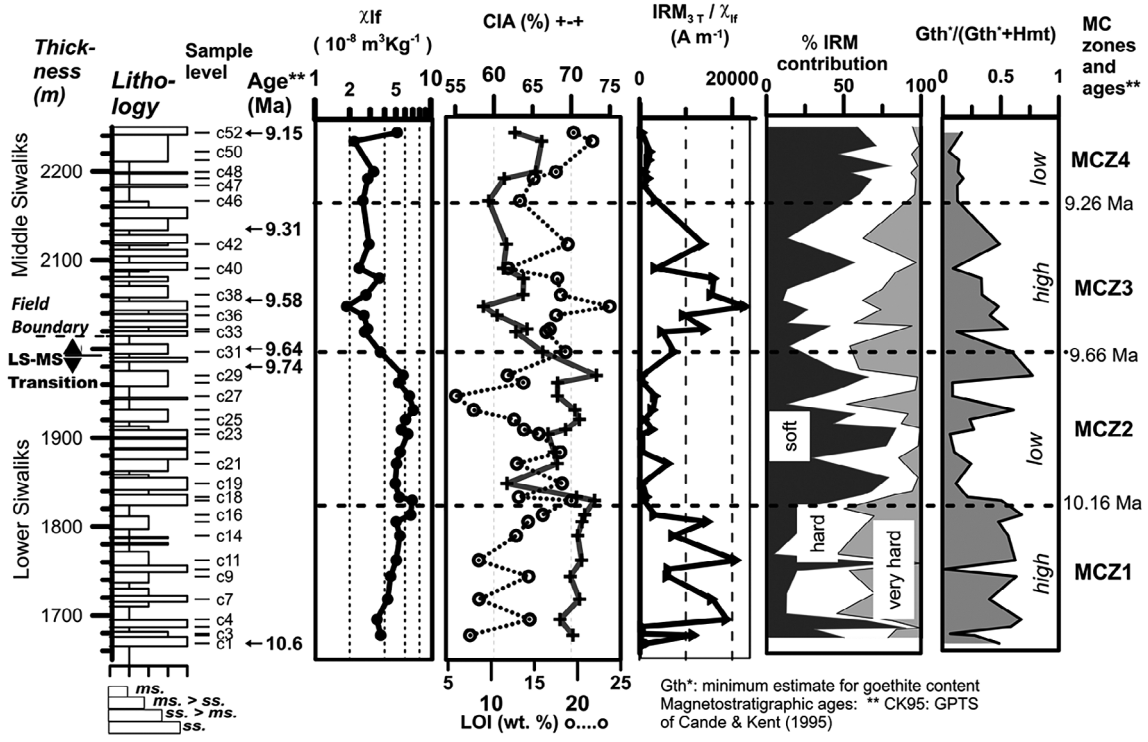

FIGURE 10 Schematic lithological column (with sample levels and magnetostratigraphic ages) and logs of various parameters: magnetic susceptibility (χlf), chemical index of alteration (CIA), loss on ignition (LOI), and magneto-mineralogical indicators (IRM3 T/χlf, %IRM contribution, Gth*/Gth* + Hmt ratio). Four magneto-chemical zones (MCZ1 to MCZ4) are discriminated. The LS–MS transition is placed at the MCZ2–MCZ3 boundary, which is the most contrasting level constrained by multiple parameters at ca. 1,997 m height (9.66 Ma according to CK95 time scale)

4.3 | Integrated vertical profiles and magneto-chemical zonation

Logs of various geochemical and rock-magnetic parameters are integrated into vertical profiles in Figure 10. The left side has three representative parameters: (a) χ_{lf}, which was found to correlate well with K/Si, Al/Si and ΣFe/Si (R^2 of 0.54, 0.59 and 0.74, respectively); (b) CIA, which broadly separates the section into two parts; and (c) LOI, which exhibits quasi-periodic oscillations of smaller wavelength due to variable amounts of carbonates, hydrous phases

associated with weathering reactions, and organic matter. The right side has three rock-magnetic parameters used as indicators/proxies for magnetic mineralogy and paleoenvironment/climate/precipitation regimes.

In Figure 10, the 1,997 m level (sample C31) clearly separates the whole section into two parts with contrasting average values. It lies in the middle of the moderately inclined step of all parameters and is the most significant transition. CIA exhibits a notable but gradual decrease in the degree of chemical alteration of rocks in the source area across this level. The lower half was inferred to reflect a longer near-surface exposure and slower erosion followed by transport, whereas the opposite (shorter exposure at the surface and rapid erosion) applies to the upper half.

The LOI (wt.%) curve exhibits oscillations that mainly reflect carbonate content in several layers of marly sediments. The total IRM to χ_{lf} ratio varies markedly along the section because of the fluctuations in concentration of different types of magnetic minerals, each with a characteristic IRM component (Figure 8) and grain-size range. Profiles of magnetic and geochemical parameters (described in Section 4.1 and plotted in Figure 10) reveal three additional levels at 1683.4 m, 1831.4 m, and 2,142.4 m that exhibit intermediate values within the descending or ascending segments. Thus, three relatively complete intervals measuring 148 m, 165.3 m, and 145.7 m, respectively, and one incomplete interval of 101.2 m, bounded by these levels from bottom to top, constitute separate magneto-chemical zones (MCZ1 to MCZ4).

As mentioned in Section 2, the ages of major boundaries were determined using two timescales (CK95 and ATNTS2004), but for clarity, Figure 10 shows only CK95 ages for well-constrained chron boundaries (left) and MCZ contacts (right). The LS–MS transition corresponds to 9.66 Ma (CK95) or 9.82 Ma (ATNTS2004), the difference arising from age discrepancies in the reversal boundaries of several polarity chrons between C5n2n and C4An in the two timescales, and the presence of short reverse polarity subchrons or cryptochrons (C5n.2n-1, C5n.2n-2, C5n2n-3) in CK95 but not in ATNTS2004.

5 | INTERPRETATION AND DISCUSSION

With significant contrasts in geochemical parameters (e.g., CIA) and magnetic susceptibility, MCZ2–MCZ3 is the most distinctive transition, roughly subdividing the whole subsection into two parts (Figure 10, left). The transitional boundaries from MCZ1 to MCZ2 and MCZ3 to MCZ4 differentiate the subsection by the magnitudes of several other parameters (Figures 6, 7, 10).

The "effective magnetite" content, proportional to the soft IRM, within MCZ1 and MCZ3 is almost twice that for MCZ2 and MCZ4. It determines the share of total IRM3T/χ_{lf} and its fluctuations (Figure 10, middle and right parts). The haematite content, proportional to hard IRM, shows identical behaviour. The goethite content is about 2.5 times higher than the haematite content in odd zones but negligible in even zones (MCZ2 and MCZ4). As a result, the combined haematite and goethite content largely differs among the odd- and even-numbered zones. The elevated concentrations of intermediate and hard-coercivity minerals in odd zones enhance the saturation IRM.

Our interpretation is that the odd zones enriched in goethite relative to the total "goethite and hematite" point to a source with wetter and cooler paleoenvironments characterized by higher precipitation, but the even zones imply a drier and warmer source with lower precipitation (Abrajevitch et al., 2009; Kampf & Schwertmann, 1983; Maxbauer, Feinberg, & Fox, 2016; Sangode & Bloemendal, 2004). Thus, the MCZ1–MCZ4 sequence represents two consecutive cycles of sediment source environments. Differences in the relative contributions of magnetite-like and goethite phases lead to a distinct zonation. Each of the three complete MCZs is 153 m thick on average and 0.45 myr (after CK95) in duration, indicative of an average sediment accumulation rate (SAR) of 34.2 cm/kyr. The duration of each zone (ca. 400 kyr) coincides with the Earth's eccentricity cycle inferred also in Miocene sediments with similar sources and settings (Abrajevitch et al., 2009; Tiwari, 1987), but the short duration of the present subsection and lack of supporting data on climate proxies prevent us from further verification of this inference.

The MCZ2 to MCZ3 transition centred at the 1,997 m level marks a significant decrease in the degree of chemical alteration or weathering in the source area (Figures 4, 5, 10), and a climatic shift from drier and warmer to wetter and cooler conditions associated with enhanced monsoon precipitation (Figure 10). The vertical separation between the transitional contact and the field LS–MS boundary is 18 m, which may be considered as the maximum half-width of the transition zone (Figures 2, 10). Another minimum estimate for the thickness of the transition zone is 17.2 m, derived from the separation of C30 and C32 displaying contrasting susceptibility (κ_{lf}) values (Gautam et al., 2000). With a SAR of 34.2 cm/kyr mentioned above, this 17.2 to 36 m (full-width) range for the estimated thickness of the transition zone corresponds to 59–123 kyr. We infer this time span to be the possible parameter-dependent estimate of lag time between uplift (surface exposure of the gneisses in the source area) and deposition of coarse clastic sediments to full extent in the basin following a series of intermediate processes (enhanced precipitation, erosion, and transportation to the foreland).

6 | CONCLUSIONS

Integrated rock-magnetic and geochemical investigations of the LS–MS transition zone in the Karnali River section led to the following conclusions.

1. The LS–MS transition exhibits a distinct magneto-chemical signature recorded by four magneto-chemical zones (MCZ1–4), each about 400 kyr in duration. In contrast to the even zones, the odd zones are enriched in antiferromagnetic minerals (haematite and goethite), with a higher share of goethite implying wetter, cooler conditions with stronger precipitation in the source area.

2. The MCZ2–MCZ3 contact, situated 18 m below the field LS–MS boundary, is a prominent physico-chemical marker of the climate shift (drier and warmer to wetter and cooler conditions) and change from intense chemical alteration/weathering to physical erosion in the hinterland causally linked to climatic forcing.
3. The LS–MS transition zone, characterized by intermediate values of physico-chemical parameters, is several tens of meters thick and occupies a minimum duration of 59 kyr. It precedes the field LS–MS boundary placed at the base of thick spss.

Demarcation and dating of the zonation pattern and major transitions in other well-dated sections based on similar physico-chemical signals will help in refining geological maps, more precisely correlating the Siwalik units, and constraining the expected diachronism of major lithologic boundaries due to basin response to climatic forcing, the strength of the east–west climatic gradient and the catchment size. The integrated field- and laboratory-based data will contribute to a better understanding of the interactions among monsoon precipitation and the tectonic/structural evolution of the Himalayan range with reference to erosional processes.

ACKNOWLEDGEMENTS

We are grateful to P. Rochette and F. Vadeboin for access to the paleomagnetic laboratory and advice during measurements at CEREGE, France. We thank Matthew H. Dick from Hokkaido University for kind suggestions to improve English grammar. We acknowledge the support of Ian Somerville and Krishnan Sajeev (the journal editors) through constructive comments that helped to improve this manuscript. This study was done under a collaborative program between Tribhuvan University (Kirtipur), Hokkaido University (Sapporo), and the University of Joseph Fourier (Grenoble), where PG received research fellowships from both CNRS and Region Rhone Alpes. The authors declare that there are no conflicts of interest of any form.

ORCID


Pitambar Gautam https://orcid.org/0000-0001-8297-4359

REFERENCES

Abrajevitch, A., van der Voo, R., & Rea, D. K. (2009). Variations in relative abundances of goethite and hematite in Bengal Fan sediments: climatic vs. diagenetic signals. *Marine Geology*, *267*, 191–206. https://doi.org/10.1016/j.margeo.2009.10.010

Appel, E., Rösler, W., & Corvinus, G. (1991). Magnetostratigraphy of the Miocene-Pleistocene Surai Khola Siwaliks in west Nepal. *Geophysical Journal International*, *105*, 191–198.

Baral, U., Lin, D., & Chamlagain, D. (2017). Detrital zircon ages and provenance of Neogene foreland basin sediments of the Karnali River section, Western Nepal Himalaya. *Journal of Asian Earth Sciences*, *138*, 98–109.

Barros, A. P., Joshi, M., Putkonen, J., & Burbank, D. W. (2000). A study of the 1999 monsoon rainfall in a mountainous region in central Nepal using TRMM products and rain gauge observations. *Geophysical Research Letters*, *27*(22), 3683–3686. https://doi.org/10.1029/2000GL011827

van der Beek, P., Litty, C., Baudin, M., Mercier, J., Robert, X., & Hardwick, E. (2016). Contrasting tectonically driven exhumation and incision patterns, western versus central Nepal Himalaya. *Geology*, *44*, 327–330.

van der Beek, P., Robert, X., Mugnier, J. L., Bernet, M., Huyghe, P., & Labrin, E. (2006). Late Miocene - Recent exhumation of the central Himalaya and recycling in the foreland basin assessed by apatite fission-track thermochronology of Siwalik sediments, Nepal. *Basin Research*, *18*, 413–434.

Bernet, M., van der Beek, P., Pik, R., Huyghe, P., Mugnier, J. L., Labrin, E., & Szulc, A. (2006). Miocene to Recent exhumation of the central Himalaya determined from combined detrital zircon fission-track and U/Pb analysis of Siwalik sediments, western Nepal. *Basin Research*, *18*, 393–412.

Buggle, B., Glaser, B., Hambach, U., Gerasimenko, N., & Markovic, S. (2011). An evaluation of geochemical weathering indices in loess–paleosol studies. *Quaternary International*, *240*, 12–21. https://doi.org/10.1016/j.quaint.2010.07.01

Burbank, D. W., Beck, R. A., & Mulder, T. (1996). The Himalayan Foreland. In A. Yin & T. M. Harrison (Eds.), *Asian tectonics* (pp. 149–188). Cambridge: Cambridge University Press.

Cande, S. C., & Kent, D. V. (1995). Revised calibration of the geomagnetic polarity timescale for the Late Cretaceous and Cenozoic. *Journal of Geophysical Research*, *100*, 6093–6095.

Chirouze, F., Dupont-Nivet, G., Huyghe, P., van der Beek, P., Chakraborti, T., Bernet, M., & Erens, V. (2012). Magneto-stratigraphy of the Neogene Siwalik Group in the far eastern Himalaya: Kameng section, Arunachal Pradesh, India. *Journal of Asian Earth Sciences*, *44*(C), 117–135. https://doi.org/10.1016/j.jseaes.2011.05.016

Clift, P. D., Hodges, K. V., Heslop, D., Hannigan, R., Van Long, H., & Calves, G. (2008). Correlation of Himalayan exhumation rates and Asian monsoon intensity. *Nature Geoscience*, *1*, 875–880.

Corvinus, G. (1988). The Mio-Plio-Pleistocene litho- and biostratigraphy of the Surai Khola Siwaliks in West Nepal: first results. *Comptes Rendus de l'Académie des Sciences, Paris*, *306*(2), 1471–1477.

Coutand, I., Barrier, L., Govin, G., Grujic, D., Hoorn, C., Dupont-Nivet, G., & Najman, Y. (2016). Late Miocene-Pleistocene evolution of India-Eurasia convergence partitioning between the Bhutan Himalaya and the Shillong plateau: New evidences from foreland basin deposits along the Dungsam Chu section, Eastern Bhutan. *Tectonics*, *35*(12), 2963–2994. https://doi.org/10.1002/2016TC004258

Cullers, R. L. (2000). The geochemistry of shales, siltstones and sandstones of Pennsylvanian-Permian age, Colorado, USA: Implications for provenance and metamorphic studies. *Lithos*, *51*, 181–203.

Delcaillau, B., Hérail, G., & Mascle, G. (1987). Evolution geéomorphos-structurale de fronts de chevauchements actifs: le cas des chevauchements intra-Siwalik du Népal central. *Zeitschrift fur Geomorphologie Neue Forschung*, *31*, 339–360.

Dettman, D. L., Kohn, M. J., Quade, J., Ryerson, F. J., Ojha, T. P., & Hamidullah, S. (2001). Seasonal stable isotope evidence for a strong Asian monsoon throughout the past 10.7 m.y. *Geology*, *29*, 31–34.

Dhital, M. R. (2015). *Geology of the Nepal Himalaya: Regional perspective of the classic collided Orogen*. Springer International Publishing Switzerland.

Dhital, M. R., Gajurel, A. P., Pathak, D., Paudel, L. P., & Kizaki, K. (1995). Geology and structure of the Siwaliks and Lesser Himalaya in the Surai Khola-Barbanda area, Mid Western Nepal. *Bulletin of the Deptartment of Geology, Tribhuvan University*, *4*, 1–70.

DMG (1978). In J. M. Tater, N. B. Kayastha, & J. N. Shrestha (Eds.), *Geological map of Nepal, scale 1:1,000,000*. Compiled by. Nepal: Department of Mines and Geology, Government of Nepal.

Dunlop, D. J., & Özdemir, O. (1997). *Rock magnetism: Fundamentals and Frontiers*. Cambridge: Cambridge University Press.

Galy, A., & France-Lanord, C. (1999). Weathering processes in the Ganges-Brahmaputra basin and the riverine alkalinity budget. *Chemical Geology*, *159*, 31–60.

Galy, A., & France-Lanord, C. (2001). Higher erosion rates in the Himalaya: Geochemical constraints on riverine fluxes. *Geology*, *29*, 23–26.

Galy, A., France-Lanord, C., & Derry, L. A. (1996). The Late Oligocene Early Miocene Himalayan belt: Constraints deduced from isotopic compositions of Early Miocene turbidites in the Bengal Fan. *Tectonophysics*, *260*, 109–118.

Gansser, A. (1964). *Geology of the Himalayas*. London: Interscience Publishers.

Garzione, C. N., Dettman, D. L., Quade, J., DeCelles, P. G., & Butler, R. F. (2000). High times on the Tibetan Plateau: Paleoelevation of the Thakkhola graben, Nepal. *Geology*, *28*, 339–342.

Gautam, P. (2008). Magnetic fabric of the Siwalik sediments (Nepal): Implications to the time-space evolution of the stress field. *Journal of Nepal Geological Society*, *38*, 39–48.

Gautam, P., & Appel, E. (1994). Magnetic-polarity stratigraphy of Siwalik Group sediments of Tinau Khola section in west central Nepal, revisited. *Geophysical Journal International*, *117*, 223–234.

Gautam, P., & Fujiwara, Y. (2000). Magnetic polarity stratigraphy of Siwalik Group sediments of Karnali River section in western Nepal. *Geophysical Journal International*, *142*, 812–824.

Gautam, P., Hosoi, A., Regmi, K. R., Khadka, D. R., & Fujiwara, Y. (2000). Magnetic minerals and magnetic properties of the Siwalik Group sediments of the Karnali river section in Nepal. *Earth Planets and Space*, *52*, 337–345.

Gautam, P., & Rösler, W. (1999). Depositional chronology and fabric of Siwalik Group sediments in central Nepal from magnetostratigraphy and magnetic anisotropy. *Journal of Asian Earth Sciences*, *17*, 659–682.

Gautam, P., Ulak, P. D., Paudayal, K. N., Gyawali, B. R., & Bhandari, S. (2012). Magnetostratigraphic dating of the prime-time sedimentary record of Himalayan tectonics and climate: new age constraints (13–10 Ma) from the Siwaliks of the Tinau Khola north section, Nepal. *Geophysical Journal International*, *190*, 1378–1392.

Glennie, K. W., & Ziegler, M. A. (1964). The Siwalik Formation in Nepal. *International Geological Congress, 22 Session Reports*, *25*, 82–95.

Govindaraju, K., & Mevelle, G. (1987). Fully automated dissolution and separation methods for inductively coupled plasma atomic emission-spectrometry rock analysis – application to the determination of rare-earth elements. *Journal of Analytical Atomic Spectrometry*, *2*, 615–621.

Herail, G., & Mascle, G. (1980). Les Siwaliks du Népal central: Structure et géomorphologie d'un piédmont en cours de déformation (The central Nepalese Siwaliks: Structure and geomorphology of an upheaving piedmont). *Bulletin de l'Association de Géographes Français*, *57*(470), 259–267.

Hirschmiller, J., Grujic, D., Bookhagen, B., Huyghe, P., Mugnier, J.-L., & Ojha, T. (2014). What controls the growth of the Himalayan wedge? Pliocene to recent shortening of the Siwalik group in the Himalayan foreland belt. *Geology*, *42*(3), 247–250. https://doi.org/10.1130/G35057.1

Huyghe, P., Galy, A., Mugnier, J.-L., & France-Lanord, C. (2001). Propagation of the thrust system and erosion in the Lesser Himalaya: geochemical and sedimentological evidence. *Geology*, *29*, 1007–1010.

Huyghe, P., Mugnier, J. L., Gajurel, A. P., & Delcaillau, B. (2005). Tectonic and climatic control of the changes in the sedimentary record of the Karnali River section (Siwaliks of western Nepal). *Island Arc*, *14*, 311–327.

Itihara, M., Shibasaki, T., & Miyamoto, N. (1972). Photogeological survey of the Siwalik ranges and the Terai plain, southeastern Nepal. *Journal of Geosciences*, *14*(4), 77–98.

Johnson, N. M., Opdyke, N. D., Johnson, G. D., Lindsay, E. H., & Tahirkheli, R. A. K. (1982). Magnetic polarity stratigraphy and ages of Siwalik Group rocks of the Potwar Plateau, Pakistan. *Palaeogeography, Palaeoclimatology, Palaeoecology*, *37*, 17–42.

Kampf, N., & Schwertmann, U. (1983). Goethite and hematite in a climosequence in southern Brazil and their application in classification of kaolinitic soils. *Geoderma*, *29*, 27–39.

Kruiver, P. P., Dekkers, M. J., & Heslop, D. (2001). Quantification of magnetic coercivity components by the analysis of acquisition curves of isothermal remanent magnetisation. *Earth and Planetary Science Letters*, *189*, 269–276.

Kutzbach, J. E., Prell, W. L., & Ruddiman, W. F. (1993). Sensitivity of Eurasian climate to surface uplift of the Tibetan Plateau. *Journal of Geology*, *101*, 177–190.

Lang, K. A., Huntington, K. W., Burmester, R., & Housen, B. (2016). Rapid exhumation of the eastern Himalayan syntaxis since the late Miocene. *Geological Society of America Bulletin*, *B31419*, 1.

Larson, K. P., Godin, L., & Price, R. A. (2010). Relationships between displacement and distortion in orogens: Linking the Himalayan foreland and hinterland in central Nepal. *Geological Society of America Bulletin*, *122*, 1116–1134.

Leland, J., Reid, M. R., Burbank, D. W., Finkel, R., & Caffee, M. (1998). Incision and differential bedrock uplift along the Indus River near Nanga Parbat, Pakistan Himalaya, from Be-10 and Al-26 exposure age dating of bedrock straths. *Earth and Planetary Science Letters*, *154*, 93–107.

Lourens, L. J., Hilgen, F. J., Laskar, J., Shackleton, N. J., & Wilson, D. (2004). The Neogene period. In F. M. Gradstein, J. G. Ogg, & A. G. Smith (Eds.), *A geologic time scale* (pp. 409–440). Cambridge: Cambridge University Press.

Lupker, M., France-Lanord, C., Galy, V., Lave, J., & Kudrass, H. (2013). Increasing chemical weathering in the Himalayan system since the Last Glacial Maximum. *Earth and Planetary Science Letters*, *365*, 243–252.

Lupker, M., France-Lanord, C., Lave, J., Bouchez, J., Galy, V., Metivier, F., … Mugnier, J. L. (2011). A Rouse-based method to integrate the chemical composition of river sediments: Application to the Ganga basin. *Journal of Geophysical Research-Earth Surface*, *116*, 24.

Maxbauer, D. P., Feinberg, J. M., & Fox, D. L. (2016). Magnetic mineral assemblages in soils and paleosols as the basis for paleoprecipitation proxies: A review of magnetic methods and challenges. *Earth-Science Reviews*, *155*, 28–48.

McLennan, S. M., Hemming, S., McDaniel, D. K., & Hanson, G. N. (1993). Geochemical approaches to sedimentation, provenance, and tectonics. In M. J. Johnson & A. Basu (Eds.), *Processes controlling the composition of Clastic sediments: Geological Society of America special papers* (Vol. 284, pp. 21–40). https://doi.org/10.1130/SPE284-p21

Medlicott, H. B. (1864). On the geological structures and relations of the southern portion of the Himalayan range between the river Ganges and Ravee. *Memoirs of Geological Survey of India*, *3*(4), 1–206.

Molnar, P., Boos, W. R., & Battisti, D. S. (2010). Orographic controls on climate and paleoclimate of Asia: thermal and mechanical roles for the Tibetan Plateau. *Annual Review of Earth and Planetary Sciences*, *38*, 77e102.

Molnar, P., & England, P. (1990). Late Cenozoic uplift of mountain ranges and global climate change: Chicken or egg? *Nature*, *346*, 29–34.

Molnar, P., England, P., & Martiod, J. (1993). Mantle dynamics, uplift of the Tibetan Plateau and the Indian monsoon development. *Reviews of Geophysics*, *34*, 357–396.

Mugnier, J. L., Baby, P., Coletta, B., Vinour, P., Bale, P., & Leturmy, P. (1997). Thrust geometry controlled by erosion and sedimentation: a view from analogue models. *Geology*, *25*(5), 427–430.

Mugnier, J. L., Delcaillau, B., Huyghe, P., & Leturmy, P. (1998). The break-back thrust splay of the main dun thrust: evidence of an intermediate displacement scale between earthquake slip and finite geometry of thrust systems. *Journal of Structural Geology*, *20*, 857–864.

Mugnier, J. L., & Huyghe, P. (2006). The Ganges basin geometry records a pre-15 Ma isostatic rebound of Himalaya. *Geology*, *34*(6), 445–448.

Munthe, J., Dongol, B., Hutchison, J. H., Kean, W. F., Munthe, K., & West, R. M. (1983). New fossil discoveries from the Miocene of Nepal include a hominoid. *Nature*, *303*, 331–333. https://doi.org/10.1038/303331a0

Najman, Y. (2006). The detrital record of orogenesis: A review of approaches and techniques used in the Himalayan sedimentary basins. *Earth-Science Reviews*, *74*(1–2), 1–72.

Nakayama, K., & Ulak, P. D. (1999). Evolution of fluvial style in the Siwalik Group in the foothills of the Nepal Himalaya. *Sedimentary Geology*, *125*, 205–224.

Nesbitt, H. W., & Young, G. M. (1982). Early Proterozoic climates and plate motions inferred from major element chemistry of lutites. *Nature*, *299*, 715–717.

Neupane, B., Ju, Y. W., Tan, F. Q., Baral, U., Das Ulak, P., & Sun, Y. (2017). Cenozoic tectonic evolution of the Tibetan Plateau - the Nepal Himalaya and the provenance of their foreland basins. *Geological Journal*, *52*, 646–666.

Ojha, T. P., Butler, R. F., DeCelles, P. G., & Quade, J. (2009). Magnetic polarity stratigraphy of the Neogene foreland basin deposits of Nepal. *Basin Research*, *21*, 61–90.

Ojha, T. P., Butler, R. F., Quade, J., DeCelles, P. G., Richards, D., & Upreti, B. N. (2000). Magnetic polarity stratigraphy of the Neogene Siwalik Group at Khutia Khola, far western Nepal. *Geological Society of America Bulletin*, *112*, 424–434.

Prell, W. L., & Kutzbach, J. E. (1992). Sensitivity of the Indian monsoon to forcing parameters and implications for its evolution. *Nature*, *360*, 647–652.

Rahman, M. J. J., & Suzuki, S. (2007). Geochemistry of sandstones from the Miocene Surma Group, Bengal Basin, Bangladesh: Implications for Provenance, tectonic setting and weathering. *Geochemical Journal*, *41*, 415–428.

Rochette, P., Mathé, P. E., Esteban, L., Rakoto, H., Bouchez, J. L., Liu, Q., & Torrent, J. (2005). Non-saturation of the defect moment of goethite and finegrained hematite up to 57 Teslas. *Geophysical Research Letters*, *32*, L22309. https://doi.org/10.1029/2005GL024196

Rösler, W., & Appel, E. (1998). Fidelity and time resolution of the magnetostratigraphic record in Siwalik sediments: high-resolution study of a complete polarity transition and evidence for cryptochrons in Miocene fluviatile section. *Geophysical Journal International*, *135*, 861–875.

Rösler, W., Metzler, W., & Appel, E. (1997). Neogene magnetic polarity stratigraphy of some fluviatile Siwalik sections, Nepal. *Geophysical Journal International*, *130*, 89–111. https://doi.org/10.1111/j.1365-246X.1997.tb00990.x

Ruddiman, W. F., & Kutzbach, J. E. (1989). Forcing of the late Cenozoic northern hemisphere climate by plateau uplift in southeast Asia and the American southwest. *Journal of Geophysical Research*, *94*(18), 409–427.

Sangode, S. J., & Bloemendal, J. (2004). Pedogenic transformation of magnetic minerals in Pliocene–Pleistocene palaeosols of the Siwalik Group, NW Himalaya, India. *Palaeogeography, Palaeoclimatology, Palaeoecology*, *212*, 95–118. https://doi.org/10.1016/j.palaeo.2004.05.019

Schatz, A.-K., Scholten, T., & Kühn, P. (2014). Paleoclimate and weathering of the Tokaj (NE Hungary) loess-paleosol sequence: a comparison of geochemical weathering indices and paleoclimate parameters. *Climate of the Past Discussions*, *10*, 469–507. https://doi.org/10.5194/cpd-10-469-2014

Schwertmann, U. (1988). Occurrence and formation of iron oxides in various pedoenvironments. In J. W. Schwertmann, B. A. Goodman, & U. Schwertmann (Eds.), *Iron in soils and clay minerals* (pp. 267–308). Norwell, MA: D. Reidel.

Sigdel, A., & Sakai, T. (2013). Petrography of Miocene Siwalik Group sandstones, Karnali River section, Nepal Himalaya: Implications for source lithology and tectonic setting. *Journal of Nepal Geological Society*, *46*, 95–110.

Sigdel, A., Sakai, T., Ulak, P. D., Gajurel, A. P., & Upreti, B. N. (2011). Lithostratigraphy of the Siwalik Group, Karnali River section, far-west Nepal Himalaya. *Journal of Nepal Geological Society*, *43*(Special Issue), 83–101.

Spicer, R. A. (2017). Tibet, the Himalaya, Asian Monsoons and Biodiversity - In what ways are they related? *Plant Diversity*, *39*, 233–244. https://doi.org/10.1016/j.pld.2017.09.001

Szulc, A. G., Najman, Y., Sinclair, H., Pringle, M., Bickle, M., Chapman, H., … DeCelles, P. G. (2006). A detrital investigation of three Siwalik sections in the Nepalese Himalaya. *Basin Research*, *18*, 375–391. https://doi.org/10.1111/j.1365-2117.2006.00307.x

Taylor, R. M., & Schwertmann, U. (1974). Maghemite in soils and its origin, I. Properties and observations on soil maghemites. *Clay Mineralogy*, *10*, 299–310.

Tiwari, R. K. (1987). Higher-order eccentricity cycles of the middle and late Miocene climatic variations. *Nature*, *327*, 219–221.

Tokuoka, T., Takayasu, K., Hisatomi, K., Yamasaki, H., Tanaka, S., Konomatsu, M., … Rai, S. M. (1990). Stratigraphy and geologic structures of the Churia (Siwalik) Group in the Tinau Khola–Binai Khola area, West Central Nepal. *Memoirs of the Faculty of Science, Shimane University*, *24*, 71–88.

Tokuoka, T., Takayasu, K., Yoshida, M., & Hisatomi, K. (1986). The Churia (Siwalik) Group of the Arung Khola Area, west-central Nepal. *Memoirs of the Faculty of Science, Shimane University*, *20*, 135–210.

Upreti, B. N. (1999). An overview of the stratigraphy and tectonics of the Nepal Himalaya. *Journal of Asian Earth Sciences*, *17*(5–6), 577–606.

Whipple, K. X. (2009). The influence of climate on the tectonic evolution of mountain belts. *Nature Geoscience*, *2*, 97–104.

Zhisheng, A., Kutzbach, J. E., Prell, W. L., & Porter, S. C. (2001). Evolution of Asian monsoons and phased uplift of the Himalaya–Tibetan plateau since Late Miocene times. *Nature*, *411*, 62–66.

SUPPORTING INFORMATION

Additional supporting information may be found online in the Supporting Information section at the end of this article.

How to cite this article: Gautam P, Huyghe P, Mugnier J-L, Regmi KR. Magneto-chemical signature of the Lower-to-Middle Siwaliks transition in the Karnali River section (Western Nepal): Implications for Himalayan tectonics and climate. *Geological Journal*. 2019;1–14. https://doi.org/10.1002/gj.3727